Atmospheric
Chemistry
and Physics
Discussions

Scattering matrices of mineral dust aerosols: a refinement of the refractive index impact

Yifan Huang[1,2], Chao Liu[1,2,*], Yan Yin[1,2], Lei Bi[3]

[1]Collaborative Innovation Center on Forecast and Evaluation of Meteorological Disasters, Nanjing University of Information Science & Technology, Nanjing 210044, China

[2]Key Laboratory for Aerosol-Cloud-Precipitation of China Meteorological Administration, School of Atmospheric Physics, Nanjing University of Information Science & Technology, Nanjing 210044, China

[3]Department of Atmospheric Sciences, Zhejiang University, Hangzhou 310027, China

Correspondence to: Chao Liu (chao_liu@nuist.edu.cn)

Abstract. Dust, as one of the most important aerosols, plays a crucial role in the atmosphere by directly interacting with radiation, while there are significant uncertainties in determining dust optical properties to quantify radiative effects and to retrieve their properties. Both laboratory and in situ measurements show variations in dust refractive indices (*RI*s), and different *RI*s have been applied in different numerical studies of model developments, aerosol retrievals, and radiative forcing simulations. This study reveals the importance of the dust *RI* for the model development of its optical properties. The Koch-fractal polyhedron is used as the modeled geometry, and the pseudo-spectral time domain method and improved geometric-optics method are combined to cover optical property simulations over the complete size range. We find that the scattering matrix elements of different kinds of dust particles are reasonably reproduced by choosing appropriate *RI*s even using a fixed particle geometry. The uncertainty of the *RI* would greatly affect the determination of the geometric model, as a change in the *RI*, even in the widely accepted *RI* range, strongly affects the appropriate shape parameters to reproduce the measured dust phase matrix elements. A further comparison shows that the *RI* influences the scattering matrix elements differently from geometric factors, and, more specifically, the P_{11}, P_{12}, and P_{22} elements seem more sensitive to dust *RI*. In summary, more efforts should be devoted to account for the uncertainties on the dust *RI* in modeling its optical properties, and the development of corresponding optical models can potentially be simplified by considering only variations over different *RI*s. Considerably more research, especially from direct measurements, should be carried out to better constrain the uncertainties related to the dust aerosol *RI*s.

1 Introduction

Atmospheric aerosols play an important role in the global radiation balance directly by scattering and absorbing incident solar radiation and indirectly by influencing cloud formation as CCN or IN (Chýlek et al., 1978; Sokolik et al., 2001; Yi et al., 2011). As a major type of aerosol, mineral dust is widely distributed in the globe, especially in arid regions. Mineral dust single-scattering properties, such as the single-scattering albedo and asymmetry factor, are fundamental not only to quantify their radiative effects, but also to develop satellite retrieval algorithms from optical observations (Kahn et al., 2005; Huang et al., 2014; Xu et al., 2017).

Several aerosol optical property databases, e.g., the Global Aerosol Data Set (GADS; Koepke et al., 1997) and the Optical Properties of Aerosols and Clouds (OPAC; Hess et al., 1998), have been built to meet the needs of aerosol remote sensing and radiation studies for all aerosols as well as for particular kinds of aerosols (Meng et al., 2010; Bi et al., 2018; Liu et al., 2019). However, for simplification, the optical properties of atmospheric aerosols are often investigated by assuming a relatively simple model, e.g., using spheres and spheroids, and this simplification has resulted in obvious errors (Mishchenko et al., 1997; Feng et al., 2009). For example, the measured phase functions of dust particles are distinctive compared with the phase functions of spherical particles at sideward and backward scattering angles (Koepke and Hess, 1988; Dobuvik et al., 2002; Nousiainen, 2009). Databases with better accuracy in characterizing dust optical properties can contribute to many aspects, such as radiative forcing calculations and remote sensing applications.

Several efforts have been devoted to studying the optical properties of dust aerosols (Bi et al., 2010; Meng et al., 2010; Ishimoto et al., 2010; Liu et al., 2013; Jin et al., 2016; Xu et al., 2017). Although it is difficult but possible to mathematically define the exact shape of an actual dust particle in numerical studies (Kahnert et al., 2014; Lindqvist et al., 2014), the use of a simplified but optically equivalent model is more convenient and doable (Nousiainen and Kandler, 2015; Liu et al., 2013). By using the measured particle size information and the assumed refractive index (RI), most studies treat the geometry as an unknown variable and look for proper geometric parameters that result in simulated optical properties consistent with measurements (Bi et al., 2010; Dubovik et al., 2006; Liu et al., 2013; Lin et al., 2018; Mishchenko et al., 1997; Osborne et al., 2011). Different nonspherical shapes have been developed and applied, such as a spheroid (Mishchenko et al., 1997; Dobuvik et al., 2002; Ge et al., 2011; Merikallio et al., 2011), an ellipsoid (Bi et al., 2009; Meng et al., 2010; Kemppinen et

Atmospheric
Chemistry
and Physics
Discussions

al., 2015), and a superellipsoid (Bi et al., 2018b). Additionally, more complex and irregular particles have also been considered, e.g., spatial Poisson–Voronoi tessellation (Ishimoto et al., 2010), Gaussian random field (GRF) particles (Grynko et al., 2013), Koch-fractal particles (Liu et al., 2013; Jin et al., 2016), and nonsymmetric hexahedra (Bi et al., 2010; Liu et al., 2014). These "irregular" geometries as well as spheroids can achieve close agreement with measurements by using

5   appropriate shape parameters or combining the results from multiple shapes, which indicates that certain geometries may be optically similar or equivalent with respect to scattering light. Nousiainen and Kandler (2015) found that scattering properties of a cube-like dust particle can be mimicked by those of spheroids with a suitable shape distribution. Liu et al. (2014) found that the surface roughness and irregularity also share an optical equivalence. Lin et al. (2018) revealed that the scattering matrix elements of different types of dust particles can be achieved by changing only two parameters to specify

10   the geometry of the superspheroids. Such "optical equivalences" are important for practical applications using dust optical properties because we can use those from a relatively simple numerical model, instead those based on the exact and actual dust particles, for downstream remote sensing and radiative transfer applications.

In addition to the particle geometry, there are also significant uncertainties related to the dust RI, which is often considered an inherent characteristic (Kahnert and Nousiainen, 2006; Stegmann and Yang, 2017), whereas much less

15   attention has been devoted during the model development. Previous studies often assumed a fixed RI during simulations of the corresponding optical properties at the interested incident wavelength. The real part (Re) of dust RI is normally set to approximately 1.5, and the imaginary part (Im) is normally set between 0.001 and 0.01 at visible wavelengths, except for hematite and magnetite (Sokolik and Toon, 1999; Volten et al., 2001; Kandler et al., 2007; Meng et al., 2010). Previous studies using both measurements and numerical investigations reveal that a relatively large variation in the RI of dust

20   materials in different regions or with different components does exist (Meng et al., 2010; Bi et al., 2011; Stegmann and Yang, 2017). Kemppinen et al. (2015) revealed that the retrieved dust RIs based on the comparisons of scattering matrices between simulations and laboratory measurements deviate from the true dust RIs.

Figure 1 shows some examples of the RIs at the visual wavelengths, and we illustrate values from various different studies, i.e., those from the GADS and the OPAC (referred to as well-accepted database values), the RI spectrum based on

25   regions and dust components (Stegmann and Yang, 2017), the estimated values given by the Amsterdam-Granada Light

Scattering Database (AGLSD, Muñoz et al., 2000; Muñoz et al., 2012; Volten et al., 2001; Volten et al., 2006), and the assumed values from different modeling studies (Bi et al., 2010; Ishimoto et al., 2010; Merikallio et al., 2011; Liu et al., 2013; Kemppinen et al., 2015). The *Re* values are mainly between 1.4 and 1.7, and the range of *Im* values cover a few orders from 0.00001i to 0.1i. The uncertainty of the *RI* is obvious, and a better understanding of the *RI* is an important prerequisite

5   for studying the optical properties of dust and its further application.

This study uses the measured dust scattering properties from the AGLSD as the reference to 'evaluate' the modeled results. However, we will not pay too much attention to the effect or performance of different geometric factors, as this topic has been covered in several previous studies. Considering the obvious uncertainties and less attention related to the particle *RI*, this study introduces the important roles of the dust *RI* in developing corresponding models for the numerical simulation

10   of their optical properties. Section 2 introduces the models considered and the computational methods applied in this study. Section 3 investigates the impacts of the *RI* on the reproduction of the optical properties of several dust particles. The effects of the *RI* on model development are revealed in Section 4, and the impacts of the *RI* and geometries on dust optical properties are compared. Section 5 concludes the work.

2 Methodology

15   This study focuses on the effects of the *RI* on modeling the dust scattering matrix elements. The Koch-fractal particle has been used as the presumed geometry (Macke et al., 1996; Falconer, 2004; Liu et al., 2013; Jin et al., 2016). The Koch-fractal particle geometry has been used to produce concave polyhedra based on tetrahedron elements of different generations and is flexible in representing both the particle overall geometries and their detailed surface structures. Macke et al. (1996) used second-generation Koch-fractal particles with different irregularities to explore the scattering properties of complex ice

20   crystals using a geometric-optics method. Liu et al. (2013) extended the applications of Koch-fractal particle geometries to mineral dust particles and found that the corresponding optical properties represent those from measurements.

Figure 2 shows three examples of third-generation Koch-fractal particle geometries. The sequential number of the Koch-fractal generation indicates the complexity of the surface structure, and an irregular ratio defines the random

movements of higher-order polyhedra to specify particle irregularity. Liu et al. (2013) introduced the aspect ratio (*AR*, the ratio of height to width) to generate prolate or oblate particles. Macke et al. (1996) and Liu et al. (2013) include more details on the definition of the Koch-fractal particles. In Figure 2, the Koch-fractal particle on the left is the nearly regular particle with an *AR* of 1.0 (1.06 for a regular particle) and an irregular ratio of 0. The middle particle has an irregular ratio of 0 but an

5   *AR* of 2.5, and the particle on the right, which is the most irregular particle, has an *AR* of 2.5 and an irregular ratio of 0.3. Previous studies indicate that geometries with proper irregularity have better potential to characterize the geometric features of several types of actual dust particles. To constrain the geometric variations considered, all particles will be the third-generation Koch-fractal particles with an irregular ratio of 0.3, and we will only consider different *AR*s in this study.

    To account for the irregular geometries, multiple numerical models are available to calculate the single-scattering

10   properties of nonspherical particles (Yang and Liou, 1996a; Mishchenko et al., 1997; Yurkin and Hoekstra, 2011; Bi et al., 2013). Following Liu et al. (2013), this study uses a combination of the pseudo-spectral time domain method (Liu, 1997; Liu et al., 2012) and the improved geometric-optics method (Yang and Liou, 1996b; Yang and Liou, 1998; Bi et al., 2014) to cover the required range of dust size parameters at visible incident wavelengths. For the irregular fractal particles, we use *r*, i.e., the radius of a volume-equivalent sphere, to define their sizes, so the size parameter *x* is defined as $x=2\pi r/\lambda$ (with λ being

15   the wavelength). Computations are carried out to cover the size distributions of several typical dust particles. After integration of the optical properties over the simultaneously measured dust size distributions (Volten et al., 2006; Muñoz et al., 2012), the resulting bulk scattering matrix elements of certain *RIs* and particle geometries can be compared with the AGLSD measurements, and the agreements between the measurements and simulations are used to specify the potentials of the corresponding methods.

20   The square values of the differences between the simulated and measured results are used as the indicator to quantify the differences between the simulations and observations. For P_{11}, the difference d_{11} is defined as Eq. (1):

$$d_{11} = \sum_{\theta=5°}^{173°} \left(\frac{P_{11}^{mea}(\theta) - P_{11}^{simu}(\theta)}{P_{11}^{mea}(\theta)} \right)^2, \tag{1}$$

where $P_{11}^{mea}(\theta)$ is the measured P_{11} element at scattering angle θ and $P_{11}^{simu}(\theta)$ is for simulated model. Note that the AGLSD provides the scattering matrix elements with scattering angles between 5° and 173°. Moreover, the difference d_{ij} of

the other five scattering phase matrix elements can be given by Eq. (2):

$$d_{ij} = \sum_{\theta=5°}^{173°} \left(\frac{P_{ij}^{mea}(\theta) - P_{ij}^{simu}(\theta)}{P_{11}^{mea}(\theta)} \right)^2 , \qquad (2)$$

where $P_{ij}^{mea}(\theta)$ and $P_{ij}^{simu}(\theta)$ are the measured and simulated elements, respectively. The numerical model that gives the smallest d_{11} will be defined as our optimal model for each dust sample, which also results in the minima of d_{12}, d_{43}, and d_{44} for most cases, and d_{22} and d_{33} are very close to their minima. We have also tried to find the minimum of the d_{ij} summation, i.e., $d_{11} + d_{12} + d_{22} + d_{33} + d_{43} + d_{44}$, as the optimal case, and very close results (a difference on Re of 0.1 or a difference on Im of $10^{-0.5}$) were obtained.

The scattering phase matrices of feldspar, quartz, loess, Lokon (volcanic ash), and red clay from the AGLSD are considered as the references, and again, this study emphasizes the role of the RI of dust. These actual dust particles have different compositions, shapes, and size distributions, which cause their unique optical properties. Therefore, by considering multiple kinds of dust particles, we attempt to demonstrate that the effects of the RI generally hold. Furthermore, the influences of particle geometries can hardly be isolated or avoided during the study, so the roles of the RI and geometry will be compared.

3 The impact of the refractive index

As discussed in Section 1, large variations in the RIs at visible wavelengths do exist for dust particles in different regions due to the differences in their components. To take advantage of the numerical investigation, we consider relatively larger ranges of RIs. The Re ranges from 1.4 to 2.2 in steps of 0.1 (9 values), and values from 10^{-4} to 10^{-2} in steps of $10^{-0.5}$ (in logarithmical scale, i.e., 5 values) are used for the Im. We mostly focus on the optical properties at an incident wavelength of 633 nm, and the spectral consistency will be briefly discussed at the end of Section 3.

Figure 3 illustrates the bulk scattering matrices of simulated Koch-fractal particles with different Re values. Third-generation Koch-fractal particles with an AR of 2.5 and an irregular ratio of 0.3 are applied. Figure 3 clearly shows that different scattering matrix elements have distinct sensitivities to the changes in the Re. The effects of Re on the P_{11} /P_{11}(30°) element mainly appear in the sideward and backward directions, and the scattering at scattering angles larger than

30° becomes stronger as Re increases. With an increase in Re, the P_{12}/P_{11} element becomes closer to zero, and the P_{22}/P_{11} element departs from 1. The differences for the other three elements, i.e., P_{33}/P_{11}, P_{43}/P_{11}, and P_{44}/P_{11}, are less significant. Another noteworthy phenomenon is that the differences between the computed scattering matrix elements with Re between 1.4 and 1.6 are more obvious than those with Re values of 2.0 and 2.2, illustrating that the scattering matrix elements are more sensitive to the changes in Re when the value of Re is relatively small (e.g., 1.4).

Figure 4 is similar to Figure 3 but for results with different Im values. Im directly affects particle absorption, but its impact on particle scattering properties cannot be ignored. We consider a dust sample with relatively larger sizes to better demonstrate the effect of the Im. The bulk scattering matrix elements are obtained based on the size distribution of Lokon samples, which have an effective radius of 7.1 µm. Again, different scattering matrix elements have distinct sensitivities to the change in the Im, and the P_{11}, P_{12}, and P_{22} elements are more sensitive to the Im. With increasing Im, the $P_{11}/P_{11}(30°)$ element decreases at scattering angles from 30° to 180°, indicating weaker side and backward scattering. The P_{22}/P_{11} element increases as the Im increases. The P_{33}/P_{11}, P_{43}/P_{11} and P_{44}/P_{11} elements show less variation for different Im values. Additionally, the scattering matrix elements change in the same directions as the Re increases or the Im decreases.

Figures 3 and 4 clearly show the impacts of the RIs on the modeling particle scattering matrix elements. With the size distribution measured simultaneously, the RI and geometry both remain variables for the numerical studies. In contrast to previous studies with a fixed RI but with variable particle shapes (Merikallio et al., 2011, 2013; Ishimoto et al., 2010; Tang and Lin, 2013; Bi and Yang, 2014; Nousiainen, 2014), this study tests whether the scattering matrix elements of different dust aerosols can be reproduced by models with a fixed particle shape but different RIs.

Figure 5 compares the simulated scattering matrices of five dust species with measurements: feldspar, quartz, loess, red clay, and Lokon (from left to right respectively). For the modeling results, a fixed geometry, i.e., the third-generation Koch-fractal particle with an AR of 2.5 and an irregular ratio of 0.3, is used for all simulations. Most of the previous numerical and observational studies suggest that the Re values lie between 1.5 and 1.6, and the scattering matrix elements are more sensitive to the Re change when the Re values are relatively small. Therefore, we include an additional Re of 1.55 in this study, which results in a total of 50 complex RIs (10 Re and 5 Im values). The blue shaded regions in Figure 5 indicate the variations in the simulated matrix elements with the 50 RIs, and the red curves correspond to the optimal cases that give

the minimum d_{11} among the 50 cases. Even with a fixed geometry, the simulated results of the five dust samples can achieve reasonable agreement with the measurements, especially for the $P_{11}/P_{11}(30°)$, P_{12}/P_{11}, and P_{33}/P_{11} elements. The modeling for feldspar, quartz, and loess are successful, and the optimal results for red clay slightly differ from the observations but still reflect the characteristics of red clay's scattering matrix. The computed results for Lokon particles achieve a relatively

5 accurate agreement with the measurements with a Re larger than expected values, i.e., 2.2. Most of the RIs obtained for the optimal cases have a real part of 1.5-1.6 and an imaginary part between 10^{-4} and 10^{-3}, consistent with generally accepted values and those suggested by the AGLSD. Table 1 lists the estimated RIs of five types of dust given by the AGLSD and the corresponding optimal RIs based on the particular geometry. It is also found that with an RI that results in the minimum value of d_{11}, the minimum values of d_{12}, d_{43}, and d_{44} are also obtained. Both the simulated and measured P_{12}/P_{11} elements

10 show considerable variations, and the simulated results match the measurements by mainly changing the real part of the RI. However, the computed and measured P_{22}/P_{11} elements show obvious differences. Both the simulated and measured P_{33}/P_{11} elements show less variation, indicating that the P_{33}/P_{11} element is less sensitive to the changes in the RI, and the simulated results with almost any RI satisfactorily agree with the measurements. The P_{44}/P_{11} elements show similar features to the P_{33}/P_{11} elements, but the consistencies between the numerical results and the measurements are slightly worse than those of the

15 P_{33}/P_{11} elements. Generally, the scattering matrices of different dust samples can be reproduced by applying proper RIs with a fixed geometry, although the differences between the simulated and measured quantity of some particular elements (e.g., the P_{22}/P_{11} elements) are noticeable, which is the same as models considering geometric variations.

Figure 6 compares the computed and measured scattering matrices of feldspar at two different incident wavelengths, in which the blue and red colors represent the results at incident wavelengths of 633 nm and 442 nm, respectively. Again, the

20 numerical results are based on the fixed Koch-fractal geometry and 50 different RIs, as mentioned above. The optimal numerical results show similar agreement with the measurements at the two wavelengths, as discussed above, i.e., close agreement for the $P_{11}/P_{11}(30°)$, P_{12}/P_{11}, P_{33}/P_{11}, and P_{44}/P_{11} elements while relatively larger differences for the P_{22}/P_{11} and P_{43}/P_{11} elements. Furthermore, the spectral differences regarding the measured P_{22}/P_{11} elements are not shown by the simulated results, while other elements show little spectral differences or agree with the simulations. The optimal cases for

25 both wavelengths correspond to the same RI of $1.55+10^{-3}$i, which indicates relatively small wavelength independence of

8

Atmospheric
Chemistry
and Physics
Discussions

Open Access

EGU

feldspar *RI*. In other words, the Koch-fractal particle applied has a clear spectral consistency for modeling dust optical properties at multiple wavelengths, which can hardly be achieved by spheroid models (Merikallio et al., 2011; Dubovik et al., 2006; Lin et al., 2018). We also compare the spectral performance for the red clay and quartz scattering matrices, and similar results (the same optimal *RI* at the two incident wavelengths) are obtained.

5   However, the results for loess and Lokon are slightly different. Figure 7 illustrates the results for the loess sample as an example. The optimal results at wavelengths of 442 nm and 633 nm correspond to *RIs* of $1.8+10^{-4}$i and $1.6+10^{-4}$i, respectively. Additionally, the consistencies of the computed and measured results at the wavelength of 633 nm are slightly better than those at the wavelength of 442 nm, especially for the forward directions of the P_{12}/P_{11} and P_{43}/P_{11} elements. For Lokon, the same real part of *RI* (*Re* = 2.2) is obtained at the two wavelengths, while the imaginary parts are slightly different

10   (10^{-3}i at 442 nm and $10^{-3.5}$i at 633 nm). This indicates that loess and Lokon may have stronger spectral differences with respect to their optical properties, which have to be considered for downstream radiative studies and remote sensing applications.

4 Refractive index *vs.* geometry

The importance of particle geometry in modeling dust optical properties has been well studied (Bi et al., 2010; Osborne et al.,

15   2011; Lin et al., 2018), and Section 3 indicates the clear role of the *RI*. Thus, with particle size relatively well constrained, it becomes interesting to investigate whether the geometry or *RI* plays the same or different roles in modeling the dust optical properties for remote sensing and radiative forcing studies.

     We first test whether different presumed *RIs* influence the determination of particle geometries for developing dust optical models. Figure 8 gives the measured and simulated scattering matrix elements of quartz, and the simulated results of

20   Koch-fractal particles with three different geometries (different *ARs* only) and two different *RIs* are illustrated. The particles with *ARs* of 0.25, 1.0, and 3.0 and the *RIs* of $1.5+10^{-3}$i (the red curves) and $1.7+10^{-3}$i (the blue curves) are used. If the quartz *RI* is assumed to be $1.5+10^{-3}$i for the numerical simulations, the modeled results based on the Koch-fractal particles with an *AR* of 1.0 agree most closely with the measurements (for almost all six elements), and those with larger (3.0) or smaller (0.25) *ARs* both depart from the measurements. However, if the *RI* is assumed to be $1.7+10^{-3}$i, then the results based on the particles

with ARs of 0.25 and 3.0 agree more closely with the measurements, except for the P_{22}/P_{11} element. Clearly, Figure 8 indicates that if different RIs are assumed, then different geometries must be applied to represent the scattering properties of actual aerosols. Similar results are obtained for the loess and red clay samples as well (not shown here). These comparisons illustrate that the RI can significantly influence the determination of appropriate geometries in modeling studies of dust

5   optical properties.

Furthermore, we directly compare the roles of the RI and geometry in reproducing dust scattering matrices. To assess the effects of the geometry, third-generation Koch-fractal geometries with different ARs and a fixed irregular ratio of 0.3 are tested. Because the AR shows the most significant influences on the scattering properties for our Koch-fractal particles, 10 different ARs (0.25, 0.5, 0.75, 1.0, 1.5, 2.0, 2.5, 3.0, 3.5, and 4.0) are considered in the tests. The RI is fixed at $1.6\pm10^{-3.5}$i

10   (close to the RIs of feldspar, quartz, loess, and red clay obtained for Figure 5). For comparison, the effects of different RIs will be illustrated by considering particles with the fixed geometry used above.

Figure 9 illustrates the scattering matrices of Lokon as well as the simulated results for particles with different ARs and RIs. The blue curves indicate the optimal case (AR=1.0) among those with different ARs and the same RI, and the red curves are for the optimal case with an RI of $2.2+10^{-3.5}$i among those with different RIs. First, we discuss the results for P_{11}. The

15   results for particles with different geometries, i.e., ARs, but a fixed RI are illustrated by the blue areas. With the RI close to the widely accepted values, the results based on any geometry differ from the measurements, especially for the values with scattering angles larger than 90°. However, the red areas can cover the measurements at the edge and indicate that simulated results with an extreme RI can better reproduce the scattering matrix of Lokon. For other elements, the optimal results, i.e., the red and blue curves, give similar agreement with the measurements, especially for the P_{33}/P_{11}, P_{43}/P_{11}, and P_{44}/P_{11}

20   elements. Overall, for the Lokon measurements, a more reasonable RI has to be used to reproduce their optical properties, and this may be the reason why few results on modeled Lokon samples have been previously published. The other features illustrated by Figure 9 are the coverage differences among the red and blue regions, which indicate the sensitivities of the particle geometry and RI. For the P_{11}, P_{12}/P_{11}, and P_{22}/P_{11} elements, the red areas clearly cover the blue ones, indicating that particles with different RIs result in larger variations in the corresponding elements than those with different geometries. The

25   P_{33}/P_{11} and P_{43}/P_{11} elements for particles with either different geometries or different RIs show similar coverages, while the

particle geometry may lead to larger variations in the P_{44}/P_{11} elements. These differences may become useful during the development of numerical dust optical models based on observed results such as the AGLSD.

Figure 10 is similar to Figure 9, except for the red clay particles. The blue curves correspond to results with an AR of 0.25, and the red curves correspond to those with an RI of $1.8+10^{-2}i$. Comparing the two optimal cases within the different ARs and RIs, the optimal results among particles with different ARs achieve a better consistency with the measurement for P_{11}, P_{22}/P_{11}, P_{33}/P_{11}, and P_{44}/P_{11}, whereas the P_{12}/P_{11} results from the RI optimal case is slightly better. The P_{43}/P_{11} element from both cases differs from the measurements. For this case, the agreement between the modeled and measured results is clearly improved by changing the particle geometry. Similar to Figure 9, Figure 10 also illustrates that the changes in the geometry and RI can provide the simulations for different scattering matrix elements with different degrees of variation.

For the results of the feldspar particles in Figure 11, the most notable feature is that the two optimal cases with different variables are highly consistent; the reproductions of the matrix elements (except P_{22}/P_{11}) are quite successful, and the simulated P_{22}/P_{11} elements of the two optimal cases both deviate from the measurement with the scattering angles between 60° and 140°. For feldspar, i.e., the most extensively studied dust sample among the AGLSD (Bi et al., 2009; Dubovik et al., 2006; Liu et al., 2013; Lin et al., 2018; Merikallio et al., 2011; Volten et al., 2001), multiple models with appropriate combinations of the particle RI and geometry all result in close agreement with measurements. Reasonable results can be obtained by merely changing the RI even if the geometry is relatively different from reality and vice versa.

Although the geometry and RI cannot be directly compared, Figures 9-11 still briefly demonstrate their differences in influencing dust scattering matrix elements, and we find that the RI plays a role as important as that of the geometry for the development of dust optical models. However, considering the irregular dust geometries, there may be countless geometry models, whereas the RI appears to be a more manageable parameter. Additionally, a proper RI is of great importance to the optical propertie simulations, while the development of geometries can be time-consuming but ineffective for some kinds of dust particles.

5 Conclusions

This study investigates the role of the RI in modeling the dust scattering matrix elements. Instead of reproducing the dust

scattering properties by building one or a group of nonspherical geometries at a fixed *RI* (that may or may not be an accurate *RI* due to its uncertainties), we emphasize the sensitivities of the scattering phase matrix on the particle *RI*. By simply changing the *RI* during the numerical modeling, it is possible to characterize the optical properties of different dust particles, even if the model geometry is fixed. As a result, it becomes possible to simplify the model developments for different

5 mineral dust particles. To be more specific, instead of constructing and testing various geometric models, using results from particles with different *RI*s but a fixed geometry can also be a solution to calculate scattering properties of dust particles at different wavelengths, which would be more flexible and computationally efficient.

As expected, if different *RI*s are considered for dust optical property simulations, the appropriate geometry that leads to the best agreement to the observation will change accordingly. By comparing the sensitivities of the dust scattering matrix

10 elements, it is noticed that the reproductions of the scattering matrix elements of different dust particles respond differently to the change in the *RI* and geometry. With a known particle size distribution, the scattering matrix of some kinds of dust (e.g., feldspar, quartz, and loess) can be well reproduced by adjusting either the *RI* or the geometry with the other parameters fixed, but those of other dust particles (e.g., red clay and Lokon) can only be reproduced by applying an extreme and fixed geometry or *RI*. As a result, more efforts should also be devoted to better constraining the particle *RI* during the development

15 of aerosol optical properties for remote sensing and radiative transfer applications.

Author contributions. YH and CL designed the study, carried out the research, and performed the numerical simulation. YH, CL, YY, and LB discussed the results and wrote the paper. All authors gave approval for the final version of the paper.

20

Competing interests. The authors declare that they have no conflict of interest.

References

Bi, J., Huang, J., Fu, Q., Wang, X., Shi, J., Zhang, W., Huang, Z., and Zhang, B.: Toward characterization of the aerosol optical properties over Loess Plateau of Northwestern China. J. Quant. Spectrosc. Ra., 112(2), 346-360, doi: 10.1016/j.jqsrt.2010.09.006, 2011

5 Bi, L., Yang, P., Kattawar, G. W., and Kahn, R.: Single-scattering properties of triaxial ellipsoidal particles for a size parameter range from the Rayleigh to geometric-optics regimes, Appl. Opt., 48, 114–126, doi: 10.1364/AO.48.000114, 2009.

Bi, L., Yang, P., Kattawar, G. W., and Kahn, R.: Modeling optical properties of mineral aerosol particles by using nonsymmetric hexahedra, Appl. Opt., 49(3), 334–342, doi: 10.1364/AO.49.000334, 2010.

10 Bi, L., Yang, P., Kattawar, G. W.: Edge-effect contribution to the extinction of light by dielectric disks and cylindrical particles, Appl. Opt., 49, 4641–4646, doi: 10.1364/AO.49.004641, 2010.

Bi, L., Yang, P., Kattawar, G. W., Hu, Y. X., B. A.: Scattering and absorption of light by ice particles: Solution by a new physical-geometric optics hybrid method, J. Quant. Spectrosc. Ra., 112, 1492–1508, doi: 10.1016/j.jqsrt.2011.02.015, 2011.

15 Bi, L., Yang, P., Kattawar, G. W., and Mishchenko, M. I.: Efficient implementation of the invariant imbedding t-matrix method and the separation of variables method applied to large nonspherical inhomogeneous particles, J. Quant. Spectrosc. Ra., 116, 169–183, doi: 10.1016/j.jqsrt.2012.11.014, 2013.

Bi, L., Yang, P., Liu, C., Yi, B., Baum, B. A., Van Diedenhoven, B., and Iwabuchi, H.: Assessment of the accuracy of the conventional ray-tracing technique: implications in remote sensing and radiative transfer involving ice clouds, J. Quant.
20 Spectrosc. Ra., 146, 158–174, doi: 10.1016/j.jqsrt.2014.03.017, 2014.

Bi, L., Lin, W., Wang, Z., Tang, X., Zhang, X., and Yi, B.: Optical modeling of sea salt aerosols: the effects of non-sphericity and inhomogeneity, J. Geophys. Res., 123, 543–558, doi: 10.1002/2017JD027869, 2018a.

Bi, L., Lin, W., Liu, D., and Zhang, K. J: Assessing the depolarization capabilities of nonspherical particles in a super-ellipsoidal shape space, Opt. Express, 26(2), 1726–1742, doi: 10.1364/oe.26.001726, 2018b.

25 Chýlek, P., Kiehl, J. T., and Ko, M. K. W.: Optical levitation and partial-wave resonances, Phys. Rev. A, 18, 2229–2233, doi:

10.1103/PhysRevA.18.2229, 1978.

Draine, B. T. and Flatau, P. J.: Discrete-dipole approximation for scattering calculations, J. Opt. Soc. Am. A, 11, 1491–1499, doi: 10.1364/JOSAA.11.001491, 1994.

Dubovik, O., Holben, B. N., Lapyonok, T., Sinyuk, A., Mishchenko, M. I., Yang, P., and Slutsker, I.: Non-spherical aerosol retrieval method employing light scattering by spheroids, Geophys. Res. Lett., 29(10), 54, doi: 10.1029/2001gl014506, 2002.

Dubovik, O., Sinyuk, A., Lapyonok, T., Holben, B. N., Mishchenko, M., Yang, P., Eck, T. F., Volten, H., Muñoz, O., Veihelmann, B., van der Zande, W. J., Leon, J.-F., Sorokin, M., and Slutsker, I.: Application of spheroid models to account for aerosol particle nonsphericity in remote sensing of desert dust, J. Geophys. Res., 111, D11208, doi: 10.1029/2005JD006619, 2006.

Falconer, K. J.: Fractal Geometry: Mathematical Foundations and Applications, Wiley, 46 (4):499, doi: 10.2307/2532125, 2004.

Feng, Q., Yang, P., Kattawar, G. W., Hsu, C. N., Tsay, S. C., and Laszlo,I.: Effects of particle nonsphericity and radiation polarization on retrieving dust properties from MODIS observations. J. Aerosol Sci., 40(9), 776–789, doi: 10.1016/j.jaerosci.2009.05. 001, 2009.

Fournier G. R. and Evans, B. T. N.: Approximation to extinction efficiency for randomly oriented spheroids. Appl. Opt., 30, 2042–2048, doi: 10.1364/AO.30.002042, 1991.

Ge, J. M., Su, J., Fu, Q., Ackerman, T. P., and Huang, J. P.: Dust aerosol forward scattering effects on ground-based aerosol optical depth retrievals, J. Quant. Spectrosc. Ra., 112(2), 310–319, doi: 10.1016/j.jqsrt.2010.07.006, 2011

Grynko, Y., Shkuratov, Y., Förstner, J.: Light scattering by randomly irregular dielectric particles larger than the wavelength, Opt. Lett., 38(23), 5153–5156, doi: 10.1364/OL.38. 005153, 2013.

Hess, M., Koepke, P., and Schult, I.: Optical properties of aerosols and clouds: The software package OPAC, B. Am. Meteorol. Soc., 79, 831–844, doi: 10.1175/1520-0477 (1998)079<0831:OPOAAC>2.0.CO;2, 1998.

Hovenier, J.W. and van der Mee, C. V.: Basic relationships for matrices describing scattering by small particles, in: Light Scattering by Nonspherical Particles, edited by: Mishchenko, M. I., Hovenier, J. W., and Travis, L. D., Academic Press,

San Diego, Chapter 3, 61–85, 2000.

Huang, J., Wang, T., Wang, W., Li, Z., and Yan, H.: Climate effects of dust aerosols over East Asian arid and semiarid regions, J. Geophys. Res., 119, 11398–11416, doi:10.1002/2014JD021796, 2014.

Ishimoto, H., Zaizen, Y., Uchiyama, A., Masuda, K., and Mano, Y.: Shape modeling of mineral dust particles for light-scattering calculations using the spatial poisson-voronoi tessellation, J. Quant. Spectrosc. Ra., 111(16), 2434–2443, doi: 10.1016/j.jqsrt.2010.06. 018, 2010.

Jin, C., Liu, C., Yin, Y., Bi, L., and Nousiainen, T.: Modeling the scattering phase matrix of red clays, Opt. Lett., 41, 4879–4882, doi: 10.1364/OL.41.004879, 2016.

Jones, D. S.: Approximate methods in high-frequency scattering, Proc. R. Soc. Lond. A, 239(1218), 338–348, doi: 10.1098/rspa.1957.0044, 1957.

Kahn, R. A., Gaitley, B. J., Martonchik, J. V., Diner, D. J., and Crean, K. A.: Multiangle imaging spectroradiometer (MISR) global aerosol optical depth validation based on 2 years of coincident aerosol robotic network (AERONET) observations, J. Geophys. Res., 110(D10), doi: 10.1029/2004JD004706, 2005.

Kahnert, M. and Nousiainen, T.: Uncertainties in measured and modelled asymmetry parameters of mineral dust aerosols, J. Quant. Spectrosc. Ra., 100(1-3), 173–178, doi: 10.1016/j.jqsrt.2005.11.035, 2006.

Kahnert, M., Nousiainen, T., and Lindqvist, H.: Review: Model particles in atmospheric optics, J. Quant. Spectrosc. Ra., 146, 41–58, doi: 10.1016/j.jqsrt.2014.02.014, 2014.

Kandler, K., Benker, N., Bundke, U., Cuevas, E., Ebert, M., Knippertz, P., Rodríguez, S., Schütz, L., and Weinbruch, S.: Chemical composition and complex refractive index of Saharan Mineral Dust at Izana, Tenerife (Spain) derived by electron microscopy, Atmos. Environ., 41(37), 8058–8074, doi: 10.1016/j.atmosenv.2007.06.047, 2007.

Kemppinen, O., Nousiainen, T., Merikallio, S., and Räisänen, P.: Retrieving microphysical properties of dust-like particles using ellipsoids: the case of refractive index, Atmos. Chem. Phys., 15, 11117–11132, doi: 10.5194/acp-15-11117-2015, 2015.

Koepke, P. and Hess, M.: Scattering functions of tropospheric aerosols: The effects of non-spherical particles, Appl. Opt., 27, 2422–2430, doi: 10.1364/AO.27.002422, 1988.

Koepke, P., M. Hess, I. Schult, and E. P. Shettle: Global Aerosol Data Set, Report No. 243, Max-Planck-Institut für Meteorologie, Hamburg, ISSN 0937-1060, 1997.

Levoni, C., Cervino, M., Guzzi, R., and Torricella, F.: Atmospheric aerosol optical properties: a database of radiative characteristics for different components and classes, Appl. Opt., 36(30), 8031–8041, doi: 10.1364/AO.36.008031, 1997.

5 Lin, W., Bi, L., and Dubovik, O.: Assessing super-spheroids in modelling the scattering matrices of dust aerosols, J. Geophys. Res., 123, 13917–13943, doi: 10.1029/2018JD029464, 2018.

Lindqvist, H., Jokinen, O., Kandler, K., Scheuvens, D., and Nousiainen, T.: Single scattering by realistic, inhomogeneous mineral dust particles with stereogrammetric shapes, Atmos. Chem. Phys., 14(1), 143–157, doi: 10.5194/acp-14-143-2014, 2014.

10 Liu, C., Panetta, R. L., and Yang, P.: Application of the pseudo-spectral time domain method to compute particle single-scattering properties for size parameters up to 200, J. Quant. Spectrosc. Ra., 113, 1728–1740, doi: 10.1016/j.jqsrt.2012.04.021, 2012.

Liu, C., Panetta, R. L., Yang, P., Macke, A., and Baran, A. J.: Modeling the scattering properties of mineral aerosols using concave fractal polyhedra, Appl. Opt., 52, 640–652, doi: 10.1364/AO.52.000640, 2013.

15 Liu, C., Panetta, R. L., and Yang, P.: The effective equivalence of geometric irregularity and surface roughness in determining particle single-scattering properties, Opt. Express, 22(19), 23620–23627, doi: 10.1364/OE.22.023620, 2014.

Liu, C., Xu, X., Yin, Y., Schnaiter, M., Yung, Y. L.: Black carbon aggregates: an optical property database, J. Quant. Spectrosc. Ra., 222, 170–179, doi: 10.1016/j.jqsrt.2018.10.021, 2019.

Liu, Q. H.: The PSTD algorithm: A time-domain method requiring only two cells per wavelength, Microw. Opt. Technol.
20 Lett., 15, 158–165, doi: 10.1002/(SICI)1098-2760 (19970620)15:33.0.CO;2-3, 1997.

Macke, A., Mueller, J., and Raschke, E.: Single scattering properties of atmospheric ice crystals. J. Atmos. Sci., 53, 2813–2825, doi: 10.1175/1520-0469(1996)0532.0.CO;2, 1996.

Meng, Z. K., Yang, P., Kattawar, G. W., Bi, L., Liou, K. N., and Laszlo, I.: Single-scattering properties of tri-axial ellipsoidal mineral dust aerosols: A database for application to radiative transfer calculations. J. Aerosol Sci., 41, 501–512,
25 doi: 10.1016/j.jaerosci.2010.02.008, 2010.

Merikallio, S., Lindqvist, H., Nousiainen, T., and Kahnert, M.: Modeling light scattering by mineral dust using spheroids: assessment of applicability, Atmos. Chem. Phys., 11, 5347–5363, doi:10.5194/acp-11-5347-2011, 2011.

Merikallio, S., Nousiainen, T., Kahnert, M., Harri, A. M.: Light scattering by the Martian dust analog, palagonite, modeled with ellipsoids, Opt. Express, 21 (15), 17972–17985, doi: 10.1364/OE.21.017972, 2013.

5   Mie G.: Beiträge zur Optik trüber Medien, speziell kolloidaler Metallösungen, Ann. Phys., 25, 377–445, doi: 10.1002/andp.19083300302, 1908.

Mishchenko, M. I., Travis, L. D., Kahn, R. A., and West, R. A.: Modeling phase functions for dustlike tropospheric aerosols using a shape mixture of randomly oriented polydisperse spheroids, J. Geophys. Res., 102(D14), 16831–16847, doi: 10.1029/96jd02110, 1997.

10 Mishchenko, M. I. and Travis, L. D.: Capabilities and limitations of a current FORTRAN implementation of the T-matrix method for randomly oriented, rotationally symmetric scatterers, J. Quant. Spectrosc. Ra., 60, 309–324, doi: 10.1016/s0022-4073(98)00008-9, 1998.

Muñoz, O., Volten, H., de Haan, J. F., Vassen, W., and Hovenier, J. W.: Experimental determination of scattering matrices of olivine and Allende meteorite particles, Astron. Astrophys., 360, 777–788, doi: 10.1046/j.1365-8711.2000.03777.x, 15   2000.

Muñoz, O., Moreno, F., Guirado, D., Dabrowska, D. D., Volten, H., Hovenier, J. W.: The Amsterdam–Granada Light Scattering Database, J. Quant. Spectrosc. Ra., 113, 565–574, doi: 10.1016/j.jqsrt.2012.01.014, 2012.

Nousiainen, T.: Optical modeling of mineral dust particles: A review, J. Quant. Spectrosc. Ra., 110, 1261–1279, doi: 10.1016/j.jqsrt.2009.03.002, 2009.

20 Nousiainen, T. and Kandler, K.: Light scattering by atmospheric mineral dust particles, in: Light Scattering Reviews 9, edited by: Kokhanovsky, A. A., Springer Praxis Books, Springer, Berlin, Heidelberg, Germany, 3–52, doi:10.1007/978-3-642-37985-7, 2015.

Osborne, S. R., Baran, A. J., Johnson, B. T., Haywood, J. M., Hesse, E., and Newman, S.: Short-wave and long-wave radiative properties of Saharan dust aerosol, Q. J. R. Meteorol. Soc., 137, 1149–1167, doi: 10.1002/qj.771, 2011.

25 Sokolik, I. N., and Toon, O. B.: Incorporation of mineralogical composition into models of the radiative properties of

mineral aerosol from UV to IR wavelengths, J. Geophys. Res., 104(D8), 9423–9444, doi: 10.1029/1998JD200048, 1999.

Sokolik, I. N., Winker, D., Bergametti, G., Gillette, D. A., Carmichael, G., and Kaufman,Y. J. et al.: Introduction to special section: outstanding problems in quantifying the radiative impacts of mineral dust, J. Geophys. Res., 106(D16), 18015–18027, doi: 10.1029/2000JD900498, 2001.

5   Stegmann, P., and Yang, P.: A regional, size-dependent, and causal effective medium model for Asian and Saharan mineral dust refractive index spectra, J. Aerosol Sci., 114, 327–341, doi: 10.1016/j.jaerosci.2017.10.003, 2017.

Tang, H. and Lin, J. Z.: Modeling of scattering properties of mineral aerosols using modified beta function, J. Geophys. Res., 118(11), 5570–5587, doi: 10.1002/jgrd.50343, 2013.

Volten, H., Muñoz, O., Rol, E., De Haan, J.F., Vassen, W., Hovenier, J.W., Muinonen, K., and Nousiainen, T.: Scattering

10   matrices of mineral particles at 442 nm and 633 nm, J. Geophys. Res., 106, 17375–17401, doi: 10.1029/2001JD900068, 2001.

Volten, H., Muñoz, O., Hovenier, J. W., and Waters, L. B. F. M.: An update of the Amsterdam light scattering database. J. Quant. Spectrosc. Ra., 100, 437–443, doi: 10.1016/j.jqsrt.2005.11.055, 2006.

Waterman, P. C.: Symmetry, unitarity, and geometry in electromagnetic scattering, Phys. Rev. D, 3, 825–839, doi:

15   10.1103/PhysRevD.3.825, 1971.

Wiscombe W. J.: Improved Mie scattering algorithms, Appl. Opt., 19, 1505–1509, doi: 10.1364/AO.19.001505, 1980.

Xu, F., van Harten, G., Diner, D. J., Kalashnikova, O. V., Seidel, F. C., Bruegge, C. J., and Dubovik, O.: Coupled retrieval of aerosol properties and land surface reflection using the Airborne Multiangle SpectroPolarimetric Imager, J. Geophys. Res., 122(13), 7004–7026, doi: 10.1002/2017JD026776, 2017.

20   Xu, G. L., Stegmann, P. G., Brooks, S. D., and Yang, P.: Modeling the single and multiple scattering properties of soot-laden mineral dust aerosols, Opt. Express, 25, A990–A1008, doi: 10.1364/OE.25.00A990, 2017.

Yang, P. and Liou, K. N.: Finite-difference time domain method for light scattering by small ice crystals in three-dimensional space, J. Opt. Soc. Am., A 13, 2072–2085, doi: 10.1364/JOSAA.13.002072, 1996a.

Yang, P. and Liou, K. N.: Geometric-optics-integral-equation method for light scattering by nonspherical ice crystals. Appl.

25   Opt., 35, 6568–6584, doi: 10.1364/AO.35.006568, 1996b.

Yang, P., Liou, K. N., and Arnott, W. P.: Extinction efficiency and single-scattering albedo for laboratory and natural cirrus clouds, J. Geophys. Res., 102, 21825–21835, doi: 10.1029/97jd01768, 1997.

Yang, P. and Liou, K. N.: Single-scattering properties of complex ice crystals in terrestrial atmosphere, Contr. Atmos. Phys., 71, 223–248, 1998.

5 Yang, P., Feng, Q., Hong, G., Kattawar, G. W., Wiscombe, W. J., Mishchenko, M. I., Dubovik, O., Laszlo, I., and Sokolik, I. N.: Modeling of the scattering and radiative properties of nonspherical dust-like aerosols, J. Aerosol Sci., 38, 995–1014, doi: 10.1016/j.jaerosci.2007.07.001, 2007.

Yi, B., Hsu, C. N., Yang, P., and Tsay, S. C.: Radiative transfer simulation of dust-like aerosols: Uncertainties from particle shape and refractive index, J. Aerosol Sci., 42, 631–644, doi: 10.1016/j.jaerosci.2011.06.008, 2011.

10 Yurkin, M. A., and Hoekstra, A. G.: The discrete-dipole-approximation code ADDA: capabilities and known limitations, J. Quant. Spectrosc. Ra., 112, 2234–2247, doi: 10.1016/j.jqsrt.2011.01.031, 2011.

Table 1: The estimated refractive index (*RI*) values given by the Amsterdam-Granada Light Scattering Database (AGLSD) and the *RI*s corresponding to our optimal numerical results.

	Feldspar	Quartz	Loess	Red clay	Lokon
Re in the AGLSD	1.5-1.6	1.54	1.5-1.7	1.5-1.7	1.5-1.6
Im in the AGLSD	10^{-3}-10^{-5}	0	10^{-3}-10^{-5}	10^{-3}-10^{-5}	10^{-3}-10^{-5}
Optimal *RI*[a]	$1.55+10^{-3}i$	$1.6+10^{-4}i$	$1.6+10^{-4}i$	$1.8+10^{-2}i$	$2.2+10^{-3.5}i$

15 a. The optimal *RI* values were based on the Koch-fractal particle geometry and the 50 different *RI* values considered in this study.
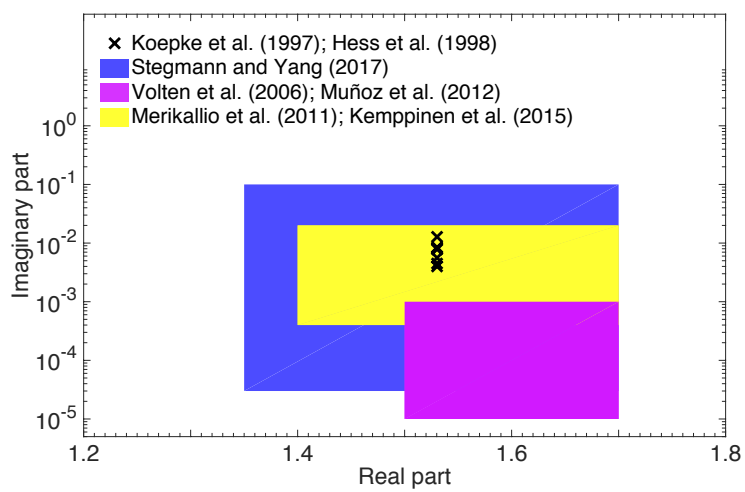
Figure 1: Refractive index from different sources.

Atmospheric
Chemistry
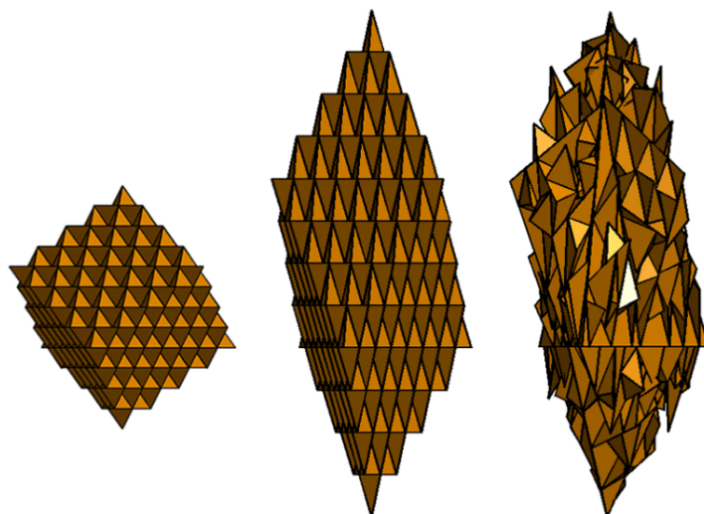and Physics
Discussions
Open Access
EGU

Figure 2: Third-generation Koch-fractal particles with different geometric parameters. The aspect ratios of the particles from left to right are 1.0, 2.5, and 2.5, and the irregular ratios are 0, 0, and 0.3, respectively.
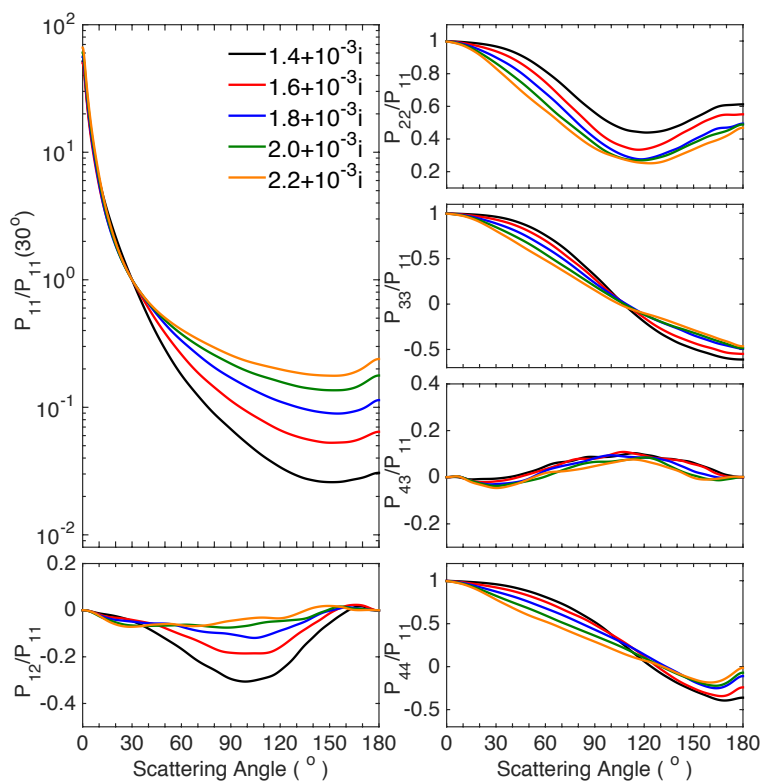
5

Figure 3: Simulated scattering matrix elements for Koch-fractal particles with different refractive indices. Here, the imaginary part is fixed at 0.001i, and the real part is changed from 1.4 to 2.2 with a step of 0.2. The particles are assumed to have the size distribution of feldspar, and the optical properties are simulated by considering an incident wavelength of 633 nm.
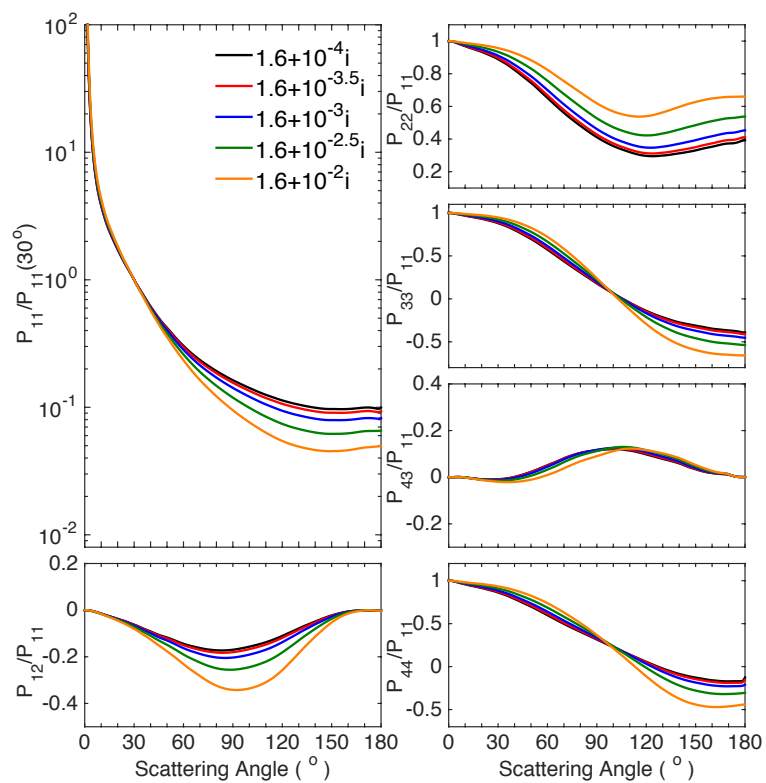
Figure 4: Similar to Figure 3, except that the real part is fixed at 1.6, the imaginary part is changed from 10^{-4} to 10^{-2} with a step of $10^{0.5}$, and the particles are assumed to have the size distribution of Lokon.
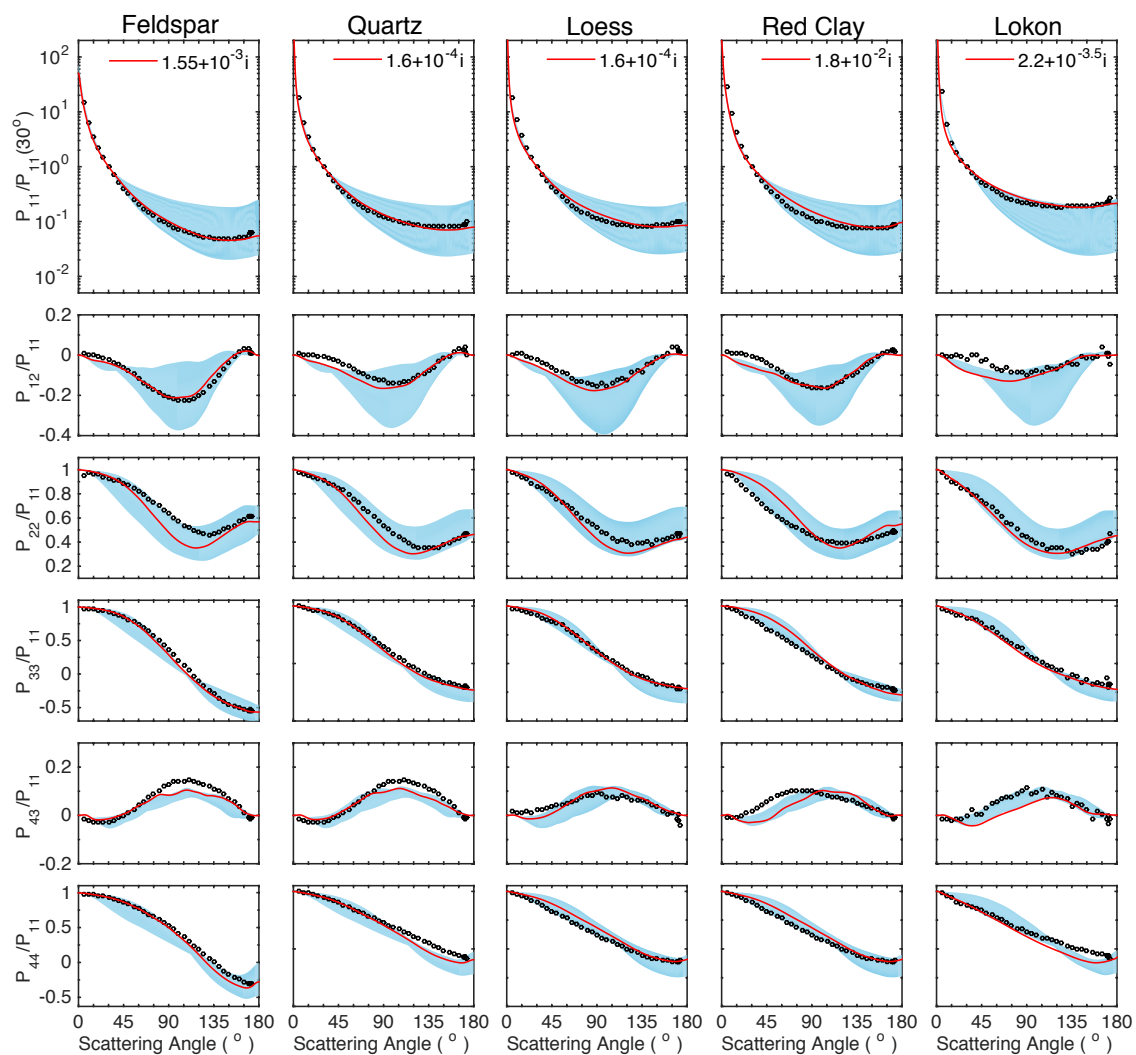
Figure 5: Comparison of the scattering phase matrix elements of feldspar, quartz, loess, red clay and Lokon particles with different refractive indices between laboratory measurements and computed results at a wavelength of 633 nm. The optimal cases are also shown as the red curves.

Atmospheric
Chemistry
and Physics
Discussions
Open Access
EGU
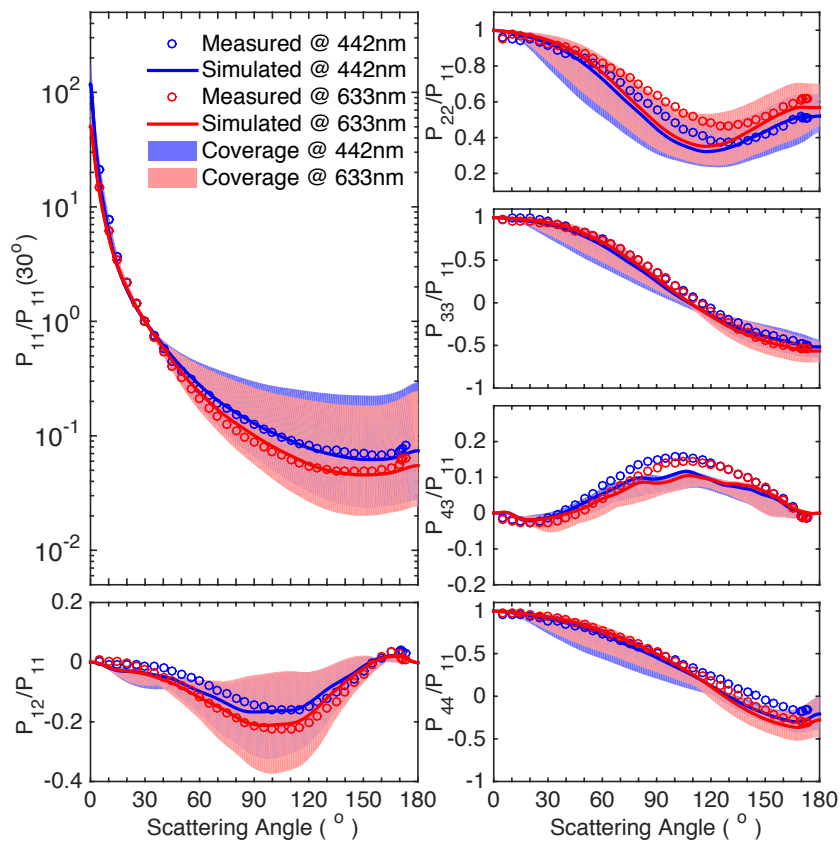
Figure 6: Comparisons of the scattering matrix elements between the measured and computed results for feldspar at wavelengths of 442 nm and 633 nm. The hallow dots indicate the measurement, the thick lines indicate the optimal computed results, and the shaded areas indicate the variety range by different _RI_s. The optimal _RI_ at both wavelengths is 1.55+10^{-3}i.
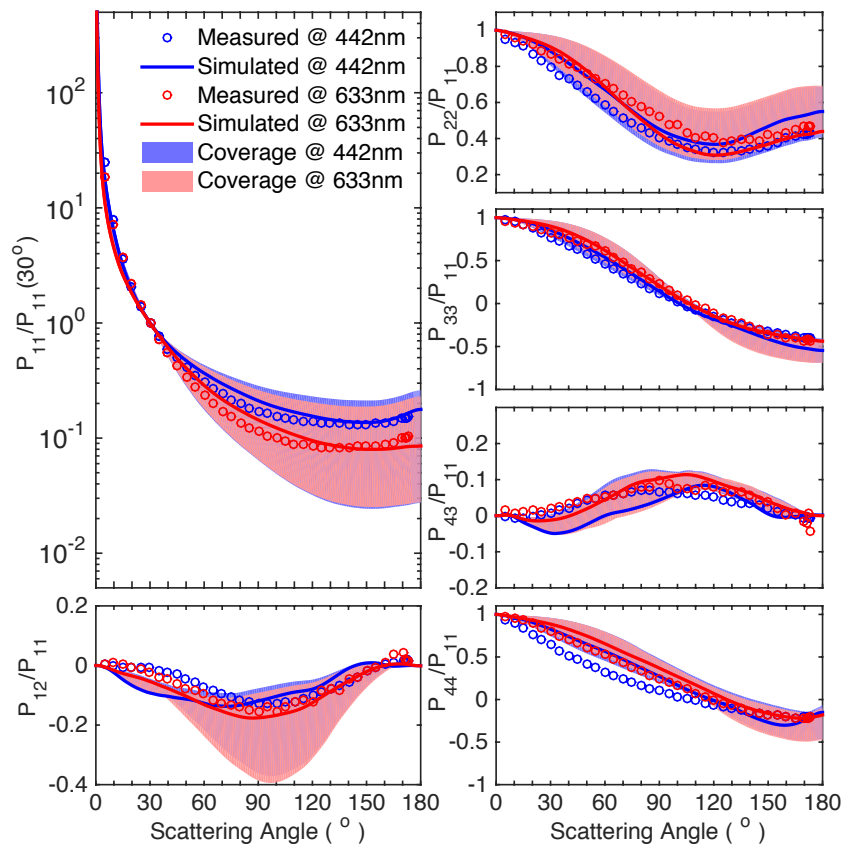
Atmospheric
Chemistry
and Physics
Discussions
Open Access
EGU

Figure 7: Similar to Figure 6, but for the loess sample. The optimal *RI* is 2.2+10^{-2}i at the wavelength of 442 nm and 1.6+10^{-4}i at the wavelength of 633 nm.

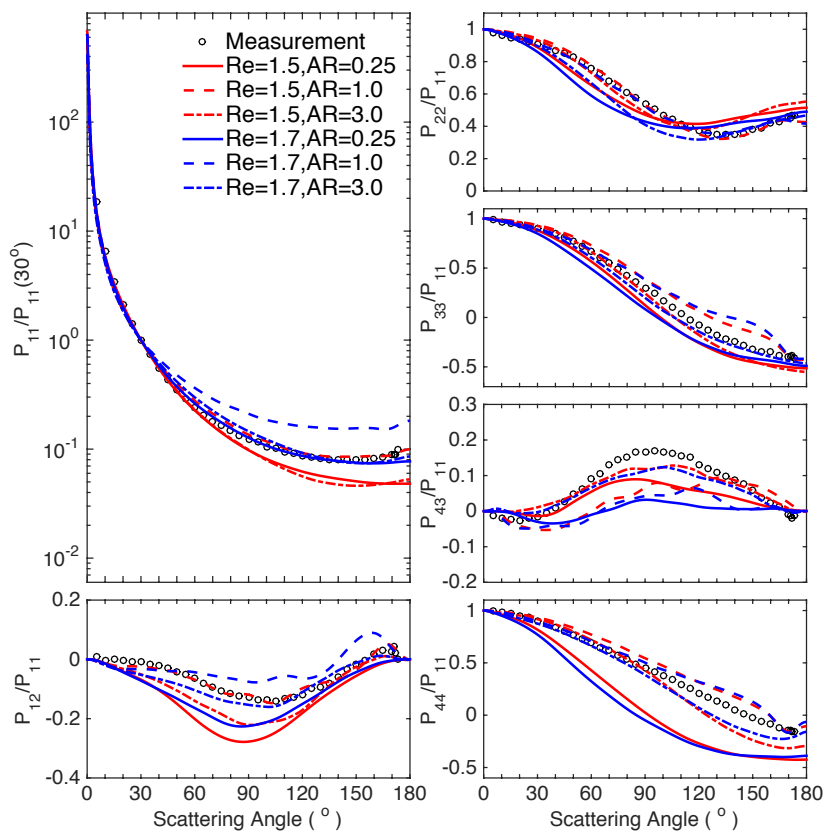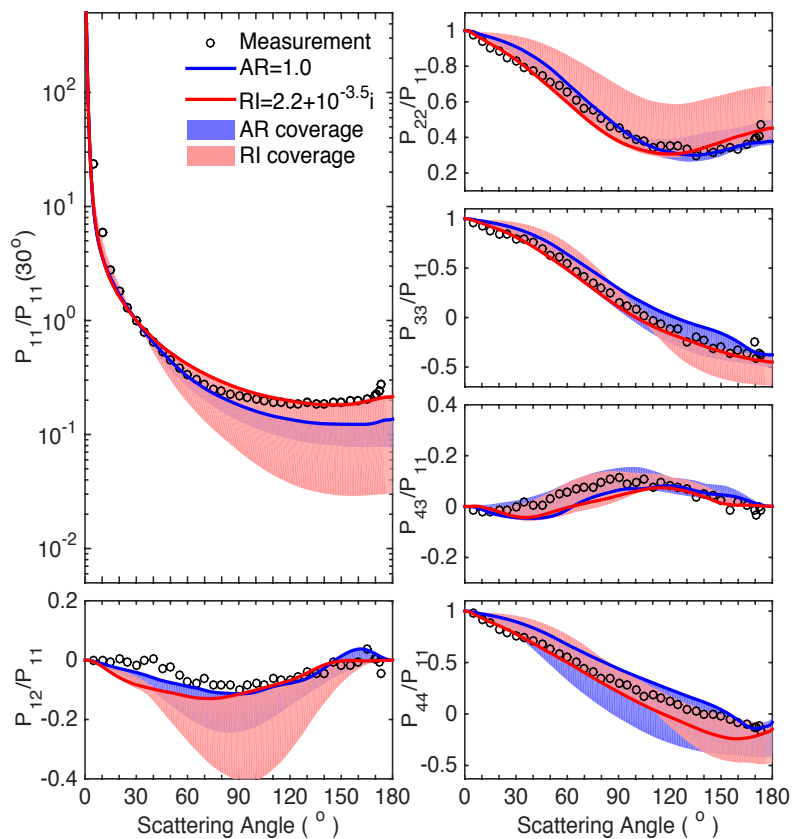Atmospheric
Chemistry
and Physics
Discussions

Figure 8: Comparison of the scattering matrix elements between the simulations and measurements for quartz samples with three different particle ARs at two different *RI*s: $1.5+10^{-3}i$ and $1.7+10^{-3}i$. The incident wavelength is 633 nm.

Figure 9: Comparison between the simulated results of the scattering phase matrix elements of the Lokon samples with different variable parameters, including coverage with the AR to be the variable (shaded blue area), coverage with the *RI* to be the variable (shaded red area), optimal case for the two variable parameters (blue and red lines) and the measurement given by the AGLSD (black hallow dots).
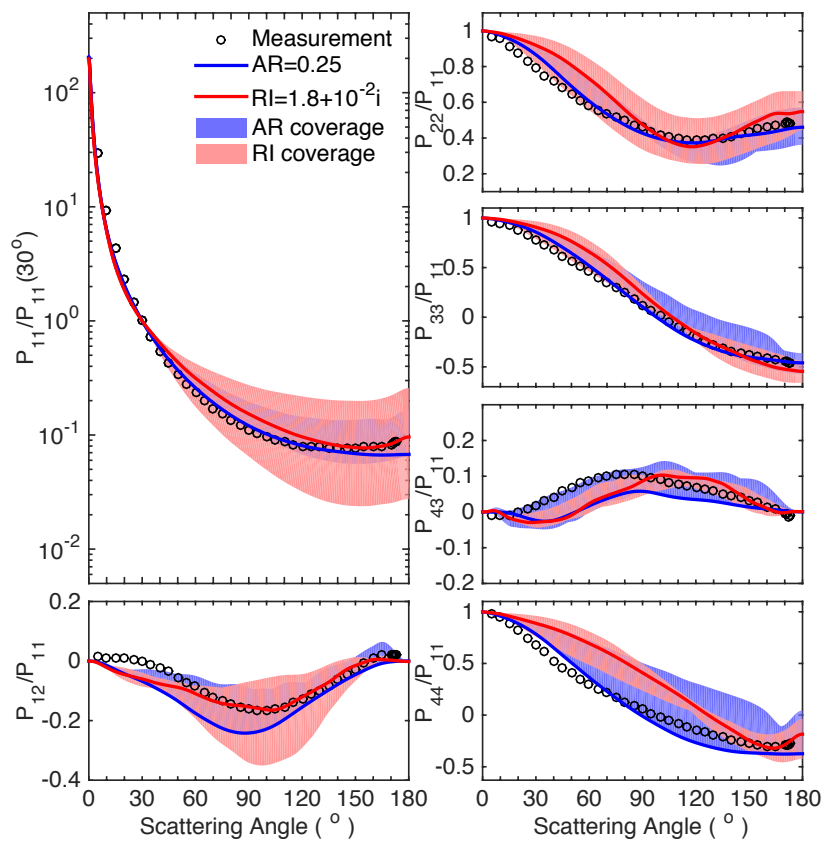
Atmospheric
Chemistry
and Physics
Discussions

Open Access
EGU

Figure 10: Similar to Figure 9 but for the red clay sample.
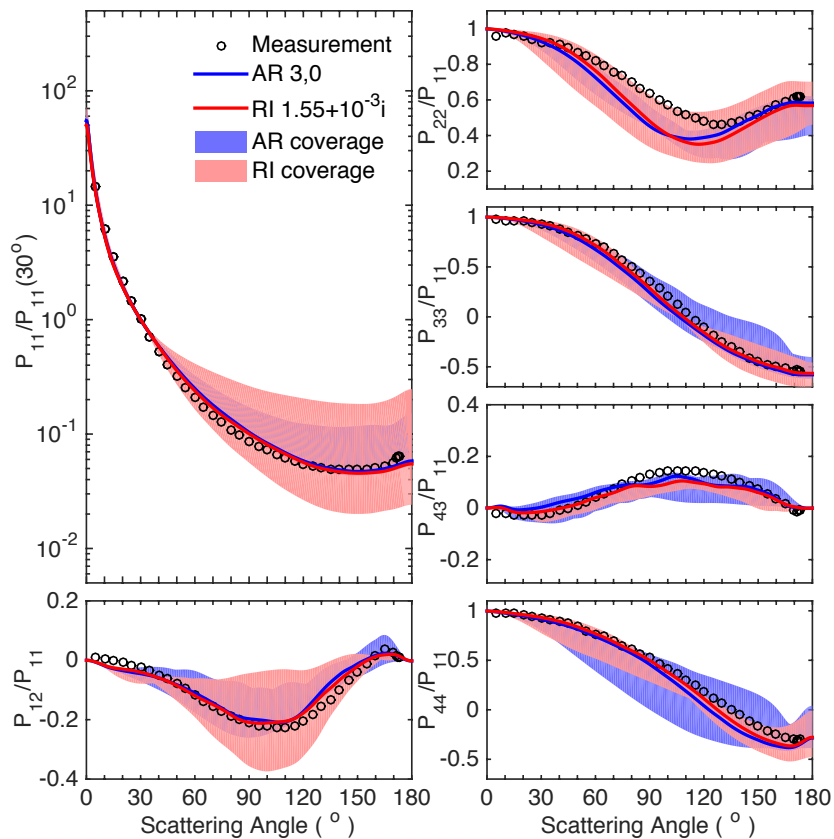
Atmospheric
Chemistry
and Physics
Discussions

Figure 11: Similar to Figure 9 and 10 but for the feldspar sample.